Materials Today Sustainability 26 (2024) 100757

Contents lists available at ScienceDirect

Materials Today Sustainability

journal homepage: www.journals.elsevier.com/materials-today-sustainability

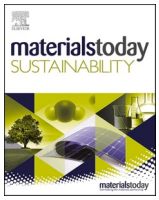

Progress in 3D printing of recycled PET

Laszlo Toth [a], Emese Slezák [b], Katalin Bocz [b,*], Ferenc Ronkay [a]

[a] Department of Innovative Vehicles and Materials, GAMF Faculty of Engineering and Computer Science, John von Neumann University, Izsáki str. 10., H-6000, Kecskemét, Hungary
[b] Department of Organic Chemistry and Technology, Faculty of Chemical Technology and Biotechnology, Budapest University of Technology and Economics, Müegyetem rkp. 3., H-1111, Budapest, Hungary

ARTICLE INFO

Keywords:
poly(ethylene terephthalate)
Recycling
3D printing
Fused filament fabrication
Toughening
Impact strength

ABSTRACT

Filaments from blends of post-industrial, low-quality recycled poly(ethylene terephthalate) (RPET) and ethylene-butyl-acrylate-glycidyl-methacrylate (EBA-GMA) were extruded with different EBA-GMA contents, then specimens were 3D-printed by fused filament fabrication technology. It has been demonstrated that, when 0–90° layer order is applied, at 15 wt% EBA-GMA content the unnotched impact strength increases by two and a half times and the notched impact strength by nine times compared to samples printed from elastomer-free RPET. DSC and DMA measurements proved that EBA-GMA reactively bonds to PET molecules, which is indicated by the increment of rigid amorphous phase and glass transition temperature and the reduction of crystallinity. The co-polymer molecules formed in-situ during compounding create a Toughening Enhancer Interphase (TEI), which also remains after 3D printing and effectively enhances impact strength. The strain at break and tensile strength of the filaments are substantially higher than that of 3D-printed specimens due to the increasing shrinkage and the resulting increased porosity of the printed specimens with higher EBA-GMA content. However, the Young-modulus values are quite similar. The flexural strength of the 3D-printed specimens reaches 40–60% of the values of injection moulded samples. The proposed method enables the production of parts with arbitrary geometry and balanced mechanical properties from RPET, which may substitute acrylonitrile butadiene styrene.

1. Introduction

The evolution of 3D printing technologies in the last couple of decades and their impact on various industrial segments are remarkable [1–4]. Nowadays, multiple 3D printing technologies are available, emphasizing FFF technology which is favorable because of its cost-efficiency and simplicity. Due to the abovementioned benefits, smaller businesses and private people can purchase it, as well, so further expansion of the supplier system is expected [5]. However, properties like dimensional accuracy, porosity, and surface roughness are often yet to be improved, as they are influenced by many parameters (nozzle temperature, flow rate, printing speed, and so on) [6–8]. Since 3D printing is still a developing science, 3D printing of nanocomposites and blends is gaining more and more attention and an increasing number of researchers are beginning to inspect this field [9–11]. Thanks to the concept of circular economy, like in the case of other polymer processing technologies [12,13], the application of recycled materials is getting increasingly important in the filament production as well [14–16]. Furthermore, the effects of several processing cycles on the mechanical and thermal properties of FFF printed polymers have been extensively investigated, too [17–21].

In the last couple of years, many researchers have experimented with recycled PET to produce filaments and 3D-printed items [15,22–32], as the high flowability and good mechanical properties (tensile and flexural modulus and strength) make it ideal for such applications. However, in many cases, the bottles were processed without grinding or compounding, and additives were not added either during the filament production, which led to much lower strength of the 3D-printed products compared to injection moulded specimens or samples cut from bottles, and did not go much beyond the poly(lactic-acid) (PLA) or poly (ethylene terephthalate glycol) (PETG) references [15,23–27,30]. Furthermore, impact strength, one of the most critical properties regarding application, was not examined at all in many studies [22–27, 30], however, some stated the printed specimens became extremely brittle, due to the moisture absorbed during processing and the high processing temperature [28]. The degradation and the crystallinity of the specimens have also not or incompletely been examined [22–31].

In our previous study [33], the filament extrusion and FFF 3D

* Corresponding author.
E-mail address: bocz.katalin@vbk.bme.hu (K. Bocz).

https://doi.org/10.1016/j.mtsust.2024.100757
Received 19 January 2024; Received in revised form 15 February 2024; Accepted 17 March 2024
Available online 24 March 2024

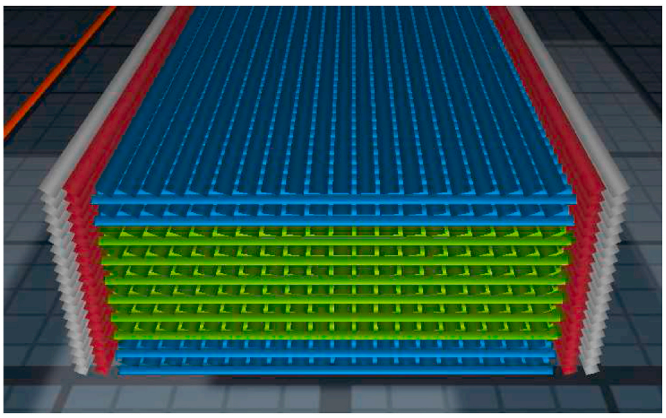

Fig. 1. Layer-order of the 3D-printed specimens.

printability of recycled and aged (in marine environment) PET flakes were investigated and it was found that the intrinsic viscosity (IV), which characterises average molecular weight, decreases more during filament production (approx. by 0.05 dl/g) compared to 3D printing (by 0.02 dl/g). The decreasing IV value refers to degradation, which is accompanied with embrittlement and reduction in impact strength.

The toughening of rigid polymers with elastomers is an increasingly spreading solution in the case of FFF 3D printing. It was successfully applied for PLA and natural rubber, as a 3.5-fold improvement was achieved in Charpy impact strength [34]. Reactive impact modifiers capable of forming covalent bonds with polymer chains can boost toughness more efficiently than non-reacting impact modifiers. Ethylene-butyl acrylate-glycidyl methacrylate (EBA-GMA) is a highly potent reactive toughener for thermoplastic polyesters as it effectively utilizes the flexibility of ethylene molecules while exhibiting good miscibility and chemical reactions with the polyester chains. Our previous research [35] compared the toughening of original (OPET) and recycled PET (RPET) with EBA-GMA. RPET appeared to be more efficient, as only 10 wt% of elastomer was enough to achieve approximately 40 kJ/m^2 Izod impact strength, while broadly similar values for OPET required twice the amount of EBA-GMA. The better compatibilization between RPET and EBA-GMA is explicable by the elevated number of end-groups (carboxyl and hydroxyl), which developed during the reprocessing. As RPET was exposed to heat and shear multiple times, the chain breakage became more pronounced and shorter chains with reactive functional groups were formed, which can develop covalent bonds with the epoxy groups of EBA-GMA. To enhance the impact properties of elastomer modified OPET blends, a small amount of recycled PET was added during reactive extrusion. Thus, a toughening enhancer interface (TEI) was formed, and the dispersion of the elastomer became more favorable. During the research, the function and evolution of TEI was also investigated [36]. By regulating the water content of PET during extrusion, hydrolytic degradation takes place and a reactive, short-chained phase – TEI – forms. By this discovery not only drying can be skipped, but improved impact strength can be achieved, as well. The role of thermal annealing on the morphological and mechanical properties of RPET-EBA-GMA blends has also been investigated [37]. The samples were heated at 150 °C for 0-20-40-60-180 s. Up to 40 s, samples with higher EBA-GMA content (15–20 wt%) showed increased impact strength due to the relaxation of RAF, but longer annealing caused a drop in impact resistance mainly because of the higher crystalline ratio. Apart from crystallinity (CRF), the ratio of the mobile (MAF) and rigid amorphous phase (RAF) also influenced the mechanical properties. This method, however, was only tested on injection moulded products in our research.

The aim of the present research is to reveal the possible advantages of using impact modified recycled PET blends in FFF process, thus giving the opportunity to transfer even low-grade PET waste into technical parts with arbitrary geometry and balanced mechanical properties. For this purpose, reactively toughened recycled PET filaments and 3D-printed samples from them were manufactured, and the effect of EBA-GMA type reactive elastomer content (in the range of 0–20 wt%) on their mechanical and morphological attributes was explored.

2. Materials and methods

2.1. Materials

Recycled PET flakes from egg-trays (provided by JP Pack, Hungary) with an IV of 0.64 ± 0.02 dl/g were used as recycled PET (RPET) material. This plastic waste is usually lower quality than bottle flakes (typically 0.72 dl/g IV values [38]), hence its recycling in the packaging industry is challenging.

Elvaloy PTW (DuPont, USA) type EBA-GMA with 5.25 wt% GMA content and a melting point of 72 °C was used as reactive elastomer at a ratio of 0-5-10-15-20 wt%.

2.2. Sample preparation

Before the filament production an LTE 26–48 (Labtech Scientific, Thailand) type twin-screw extruder was applied for compounding the blends. The PET flakes were regranulated before filament production, as the blending with the elastomer can be implemented during reactive extrusion. PET flakes were dried for 4 h at 160 °C, while the elastomer was dried at 70 °C for 4 h before compounding. The zone temperatures between the hopper and the die increased from 245 °C to 260 °C and the rotation speed of the screw was set to 20 1/min.

For the filament production a Collin Teach-Line E20T (Collin, Germany) single screw extruder was used, and the temperature of the heating zones were 240–250 °C for each composition, the screw rotation speed was 35 1/min and the fibre drawing speed was 47 1/min. During fibre drawing, the filament coming out of the extruder was cooled by being passed through a water bath. The filaments rolled up on the drum were dried at 60 °C for 24 h before printing.

A Craftbot Plus (Craftbot, Hungary) 3D-printer with open work area was applied for the printing of the specimens, equipped with all metal hot end, and the table was covered with Kapton film. The GCODE required for printing was done by a Craftware 1.23 version slicer that was developed for Craftbot+ 3D printer. The printing for each composition was done with a 250 °C head, on an 80 °C stage with a 0.4 mm nozzle. 0.2 mm layer thickness, 100% filling, 40 mm/s printing speed and 100% ventilator speed (two-sided cooling) were given in the GCODE. The specimens sufficiently adhered to the Kapton film; thus, the application of Raft was not necessary during printing, only a 5 mm offset, and 250 mm long skirt was printed around the specimens. The aim was not to maximize the mechanical properties that can be measured in one direction, therefore a 0/90° printing layer order was chosen (Fig. 1), by which the inevitably present anisotropy during FFF printing can be reduced [39]. In this way, the real conditions of application can be modelled, where typically non-uniaxial stresses occur for a particular component [40]. The colours in Fig. 1 indicate the different layers of the test specimen. Grey and red are used to indicate the outer and lateral shell layers of the specimen, blue to indicate the lower and upper shell layers, and green to indicate the inner layers. In the present case, these shell layers are irrelevant as each layer was printed with the same parameters (temperature, printing speed, fill rate). The specimens were printed with a total of 19 layers.

2.3. Methods

An RPV-1 (PSL Rheotek, UK) viscosimeter was applied to determine the intrinsic viscosity (IV) of the filaments and the 3D-printed specimens. The samples were dissolved in 60:40 wt% phenol – 1,1,2,2-tetrachloro-ethane at 100 °C, and the concentration was 0.5 g/dl. The

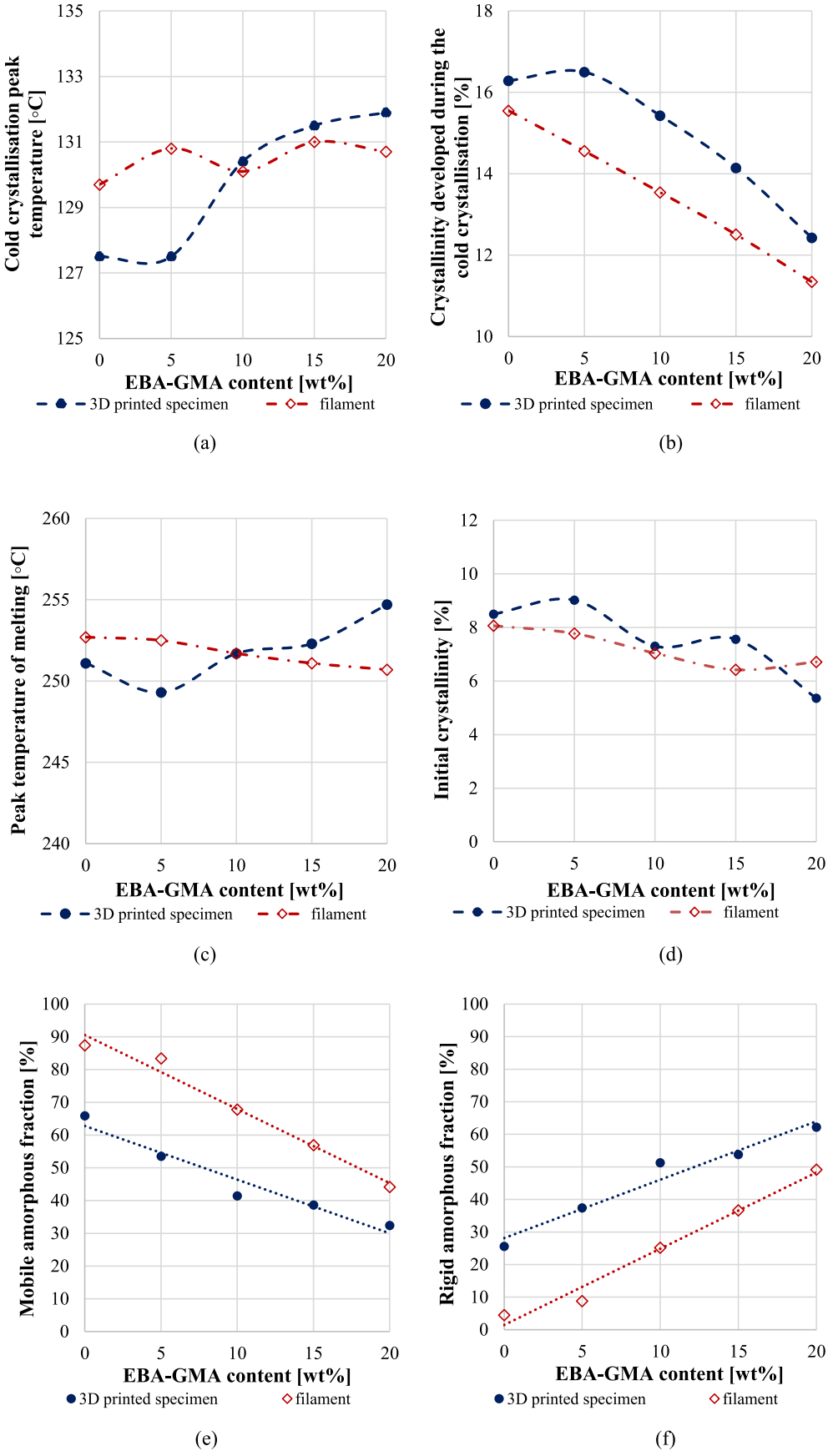

Fig. 2. Results of DSC analysis: peak temperature of cold crystallisation (**a**); peak temperature of crystalline melting (**b**); peak temperature of crystalline melting (**c**); crystalline fraction (**d**); mobile amorphous fraction (**e**) and rigid amorphous fraction (**f**) as a function EBA-GMA ratio.

Table 1
Apparent density of the samples.

	RPET + 0 wt% EBA-GMA	RPET + 5 wt% EBA-GMA	RPET + 10 wt% EBA-GMA	RPET + 15 wt% EBA-GMA	RPET + 20 wt% EBA-GMA
Filament [g/cm^3]	1.37	1.36	1.35	1.33	1.29
3D-printed sample [g/cm^3]	1.13	1.09	1.04	1.00	0.92

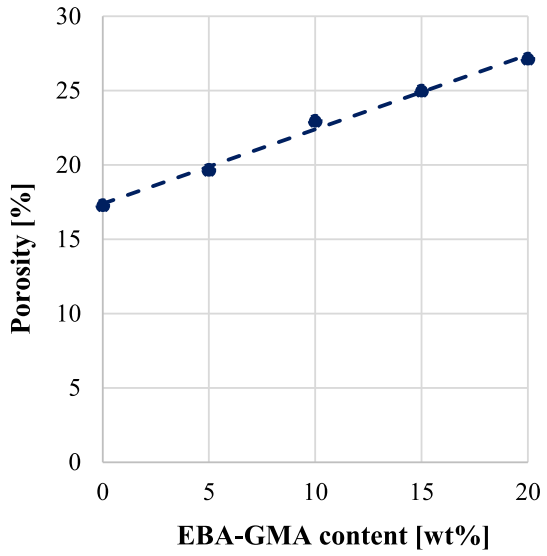

Fig. 3. Porosity of the 3D-printed specimens as a function of EBA-GMA content.

solvents were tested at 30 °C.

Both tensile and flexural tests were performed on a 3366 Universal Testing System (Instron, USA). The tensile test was carried out according to ISO 527-1 standard, using a tensile speed of 1 mm/min to determine the modulus, and subsequently tensile speeds of 50 mm/min. The flexural test was done in accordance with ISO 178 standard, at a flexural speed of 20 mm/min 5 specimens were tested for each composition.

The impact test was carried out using the Impactor II (Ceast, Italy) pendulum impactor with a 5 J non-instrumented pendulum according to ISO 179-1, starting the pendulum hammer at an angle of 150°. Both notched and unnotched samples were tested, 5 pieces for each composition.

The apparent density was calculated from the geometry and mass of the filament and 3D-printed samples based on the Archimedes method. According to this method, the approximated average porosity is calculated from Eq. (1) [41]:

$$Porosity\ [\%] = \left(1 - \frac{\frac{W_s}{V_s}}{\rho_m}\right) \times 100\%, \tag{1}$$

where W_s and V_s are the weight and bulk volume of the 3D-printed porous sample, ρ_m is the density of the solid filament material. Weight measurement was performed by a XA204 (Mettler Toledo, USA) type analytical balance. However, as data on the size, shape and distribution of the pores cannot be obtained with this method as with a CT scan [41,42] additional scanning electron microscopy was also performed.

The structure of the fracture surface after tensile test and after Izod impact test was examined by EVO MA15 (Zeiss, Germany) scanning electron microscope (SEM) after the specimen surface was coated with 5 nm gold layer. The magnifications were 60× and 1000x and the accelerating voltage was 15 kV. The working distance varied between 9 and 12 mm. Furthermore, the 3D-printed specimens were embedded in acrylic resin and polished until 3 μm surface roughness was reached. Then the elastomer phase was selectively dissolved in toluene for 1.5 h at 23 °C. The solvent residues were removed in a vacuum dryer at 60 °C and 90 mbar overnight. Prior to the examination the samples were coated with gold. 2000× magnification, 15 kV accelerating voltage and 9.5–10.5 mm working distance were chosen to examine the distribution of the elastomer phases.

The stereo-microscopic images after the flexural test were done by a Stemi 508 (Zeiss, Germany) device in a 0.63 magnification.

A DMA25 (MetraVIB, France) dynamic mechanical analyser was used in tensile test mode. The dimensions of the rectangular specimens were 18.87x4.5 × 3.7 mm. The deformation frequency was 10 Hz, and the temperature was elevated from 10 to 140 °C with 3 °C/min.

A DSC 131EVO (Setaram, France) differential scanning calorimeter was utilized to determine the ratio of the three fractions in nitrogen atmosphere. Cooling and heating rates were both 10 °C/min and the temperature changed between 30 and 300 °C. Eq. (2) was applied for the calculation of crystallinity:

$$CRF_M = \frac{\Delta h_M}{\Delta h_0 (1 - r_{EBA-GMA})} 100\%, \tag{2}$$

where CRF_M [%] is the melted crystalline fraction; Δh_M [J/g] is the detected mass-specific heat flow during melting, Δh_0 [J/g] is the mass-specific enthalpy of the entirely crystalline PET (140.1 J/g) [43]; $r_{EBA-GMA}$ [−] is the mass ratio of the elastomer. The crystallinity at cold-crystallisation was determined according to eq. (3):

$$CRF_{CC} = \frac{\Delta h_{CC}}{\Delta h_0 (1 - r_{EBA-GMA})} 100\%, \tag{3}$$

where CRF_{CC} [%] is the crystalline ratio formed at cold crystallisation; Δh_{CC} [J/g] is the mass-specific heat flow at cold crystallisation. The initial crystallinity was determined by eq. (4):

$$CRF_0 = CRF_M - CRF_{CC} \tag{4}$$

where CRF_0 [%] is the initial crystallinity of the sample.

From the DSC results the mobile amorphous phase (MAF) can be calculated, as well in accordance with eq. (5).

$$MAF = \frac{c_p}{c_p^0 (1 - r_{EBA-GMA})} 100\% \tag{5}$$

where MAF is the mobile amorphous fraction expressed in percentage [%], c_p is the specific heat change of the sample during glass transition [J/(g•K] and c_p^0 is the change in specific heat for fully amorphous PET, 0.405 J/(g•K) [43].

Knowing the two phases (CRF, MAF) the rigid amorphous fraction (RAF) can be determined according to equation (6):

$$RAF = 100\% - CRF - MAF \tag{6}$$

where RAF is the ratio of rigid amorphous phase [%].

3. Results and discussion

3.1. Degradation and crystallinity of the materials

The intrinsic viscosity (IV) of neat, recycled PET decreased from 0.64 dl/g to 0.57 dl/g during regranulation, then it further decreased to 0.51 dl/g during filament manufacturing. In the course of 3D printing, the drop in IV value of the recycled material was 0.04 dl/g. Thus, it can be concluded that the filament production causes greater degradation than printing. These IV-drops for recycled PET during the extrusion processing steps are considered to be average [33].

Fig. 2 sums up the DSC test results of the filaments and the 3D-

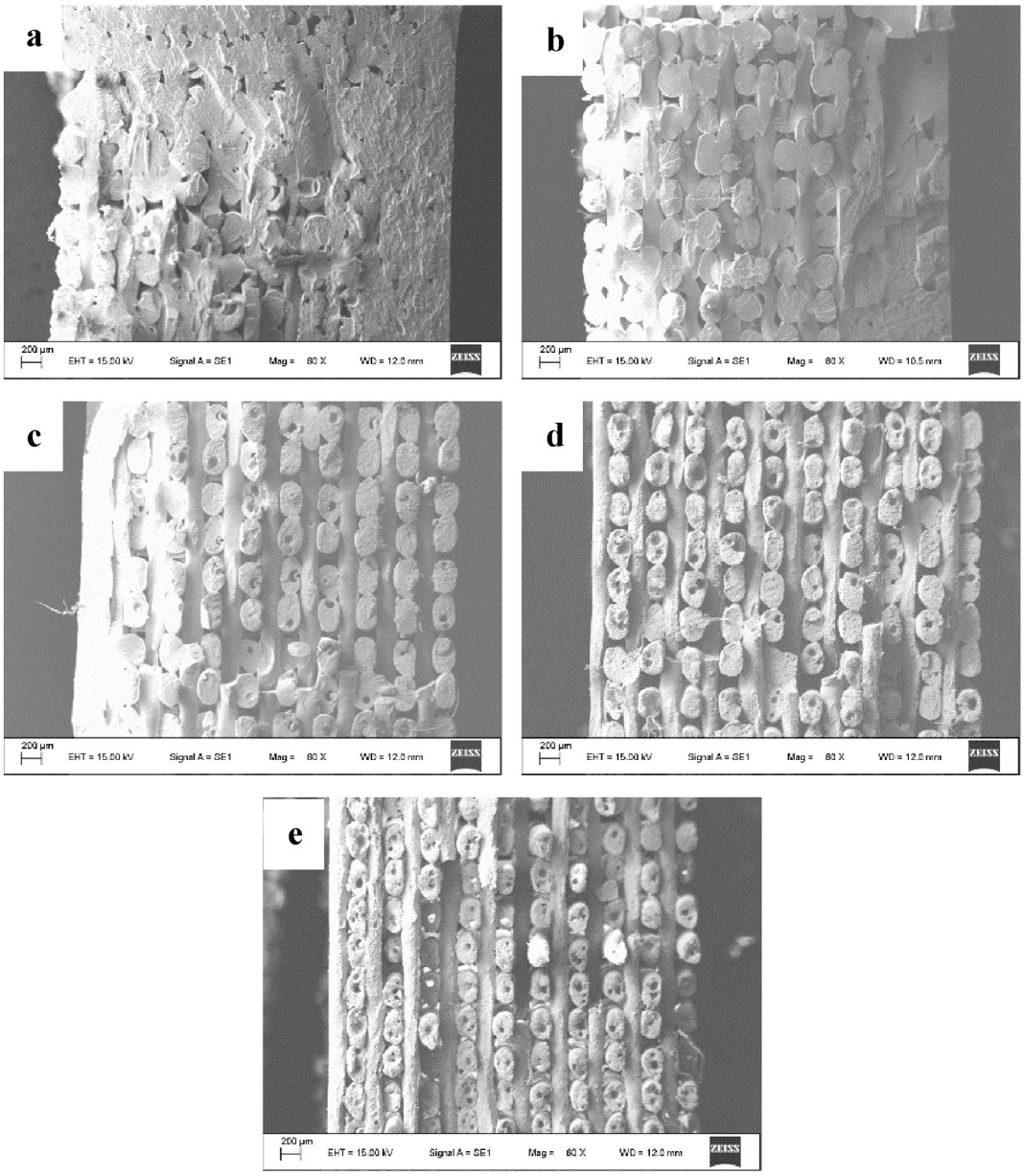

Fig. 4. SEM micrographs of fracture surface after unnotched impact test. 60× magnification (**a:** RPET; **b:** RPET+5 wt% EBA-GMA; **c:** RPET+10 wt% EBA-GMA; **d:** RPET+15 wt% EBA-GMA; **e:** RPET+20 wt% EBA-GMA).

printed specimens. It is evident that both the filaments and the 3D-printed specimens show cold-crystallisation during heating in the range of 127–132 °C. It is known from the literature that if PET is cooled rapidly after the processing steps, the formation of a high crystalline fraction can be prevented; this causes cold crystallisation on subsequent reheating [44]. Such cold-crystallisation is more pronounced in the case of 3D-printed specimens than for filaments, either way, it decreased with increasing EBA-GMA content. The rising cold-crystallisation temperature and descending ratio indicate crystallisation hindering processes caused by the EBA-GMA phase (**Fig. 2/a, b**).

During crystalline melting not only the initial crystalline phase melts, but the fraction formed in the course of cold crystallisation, which affects the melting temperature. The peak temperature of melting was between 249 and 255 °C, and with increasing elastomer content, the results slightly decreased for the filaments, while just the opposite was observed for 3D-printed specimens (**Fig. 2/c**). The initial crystallinity of the samples (CRF) was relatively low for each composition (<10%) (**Fig. 2/d**), which was caused by the rapid cooling of ventilators during filament production and printing [45]. The increasing EBA-GMA content resulted in a small fall in the initial crystalline ratio. The mobile amorphous phase (MAF) quasi linearly decreased, while the rigid amorphous fraction (RAF) showed a linear increase as the function of EBA-GMA content (**Fig. 2/e, f**). The ratio of MAF was 10–20% lower, while the RAF higher at each composition for 3D-printed specimens, compared to filaments.

The CRF-MAF-RAF results suggest that the reactive bonding of EBA-GMA and PET hinders the matrix's crystallisation and reduces the mobility of chains, which ultimately leads to the growth of RAF. Thus, RAF can form not only on the crystalline-amorphous, but the elastomer-PET interphase, too, as it was revealed in our previous study [37]. The forming TEI promotes the distribution of EBA-GMA within the recycled PET matrix.

The higher rate of cold crystallisation and higher RAF of the 3D-printed samples indicate that a greater orientation has been developed in the PET matrix. Since the diameter of the produced filament is 1.6 mm and the rasters deposited during printing are only 0.2 mm, and the flow

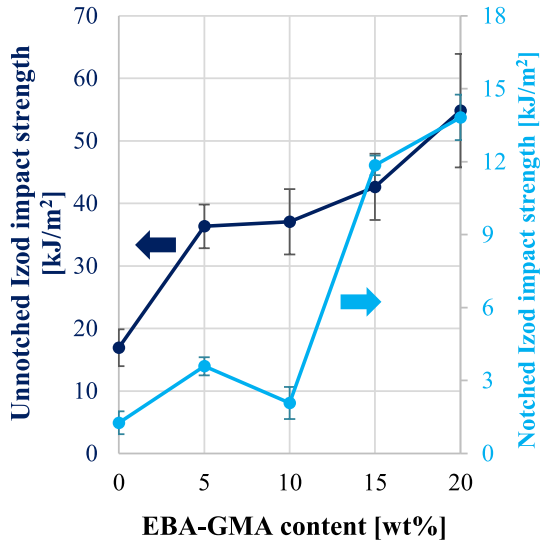

Fig. 5. EBA-GMA content dependence of unnotched and notched impact resistance.

rate during depositing is also significantly higher, a greater molecular prearrangement, orientation, may result from the greater shear.

3.2. Porosity

The porosity of the printed samples can be determined from the ratio of the apparent density of the solid filaments to that of the 3D-printed samples (**Table 1**).

This value is 17% for the toughener-free sample and shows a linearly increasing trend depending on the content of the EBA-GMA (Fig. 3).

The greater porosity indicates that there are more holes in and between the fibres. The inter and intra voids may be altered for several reasons [46]: (1) the rasters melt to different degrees when the next layer is deposited on them and deform differently; (2) the fibres shrink differently during cooling. The nominally dense FFF materials contain pores between the fibres because the filament is extruded through a circular nozzle and the resulting deposited beads cannot completely fill the volume of the CAD design [47]. Fig. 4 shows the cross sections of the samples after Izod impact test. It can be seen that the volume of inter voids is roughly similar in the cases of different EBA-GMA content. Printing with a larger nozzle diameter might help to increase the width of the fibres, thereby reducing the voids between them [48,49]. However, a larger fibre cross-sectional area may increase the proportion of intra voids, which tends to increase as a function of EBA-GMA content. As the outer surface of the fibres cools and solidifies, shrinkage of the core area can lead to the formation of voids. Some of these voids may also originate from the trapped gases that form during filament production [50]. The DSC tests show that the melting temperature of the 3D-printed samples increases slightly, which may result in a smaller fusion with increasing EBA-GMA content, using the same printing settings.

3.3. Mechanical properties of filaments and 3D-printed specimens

The impact test results of the unnotched and notched specimens are presented in **Fig. 5**. PET, as a pseudo-tough material, is prone to shear yielding, so a lot of energy is required for the initiation of cracks, but less for their propagation, which is why their unnotched impact strength is usually high, but the notched impact resistance is small [17]. This can be seen in the present case for neat material, as well. It can be observed that the unnotched impact strength doubles at 5 wt% EBA-GMA content and triples at 20 wt% EBA-GMA ratio. The changes are even greater in the case of the notched impact test: at 15 wt% EBA-GMA content a sudden increase can be observed, and the impact strength increases to its nine-fold. This shows that EBA-GMA effectively inhibits crack propagation and helps matrix yielding as the main energy dissipative process. It should be noted that these results are lower in absolute values [35], as Izod impact strength of 40–50 kJ/m^2 was also reached with similarly composed but injection moulded and therefore compact, homogeneous, and quasi-isotropic samples; but the relative increase compared to the toughener-free reference was similar.

SEM images with high magnification of the fracture surfaces formed after the notched impact test are presented in **Fig. 6**. As for the toughener-free and 5 wt% EBA-GMA containing samples, the fusion between the rasters/layers are greater than at higher elastomer ratios. As the EBA-GMA ratio increases, the raster/layer bonding weakens, presumably for two reasons: firstly, above 5 wt% EBA-GMA content, the elastomer increases the melting temperature of the 3D-printed samples, which reduces the back-melting of the previous layer when a new layer is deposited, thus weakening the bonding; and secondly, the increased EBA-GMA content may hinder the diffusion of PET molecules at the interphase.

At 10, 15 and 20 wt% elastomer contents, larger distances between the rasters and lunkers can be observed within the fibres, which indicate greater shrinkage. These results are consistent with higher porosity with increasing EBA-GMA content. In the SEM images with higher magnification, the fracture surface of the samples without elastomer and with 5 wt% EBA-GMA content is brittle, and that of the samples with higher elastomer content is ductile.

The SEM micrographs of the embedded and selectively dissolved 3D-printed specimens are presented in **Fig. 7**. Based on the images, the distribution of the elastomer particles is uniform both by size and by location, indicating that the reactive extrusion was successful. This is in good agreement with previous research results, where the good distribution of EBA-GMA due to the resulting TEI greatly contributed to the increase in impact strength [35,51,52].

Fig. 8 summarises the tensile test results**. Fig. 8/a** illustrates the typical tensile curves, and the mechanical properties calculated from the diagrams are presented in **Fig. 8 b, c, d**. The tensile strength of the toughener-free filaments is 48 MPa, which shows a decrease of 18% at 5 wt% EBA-GMA, but only a slight drop with the further increment of the elastomer ratio. The tensile strength of the 3D-printed samples is lower than that of their filaments (**Fig. 8/b**). One of the main reasons for this is that the layer order used in 3D printing not only includes a printing direction parallel to the load, but also includes layers perpendicular to it. Tsai et al. [53] measured similar tensile strength at longitudinal orientation (0°) for PET filament and test specimens printed from it. In general, compared to the 0° orientation (direction parallel to the load), the 90° samples (direction perpendicular to the load) achieve only 15–40% tensile strength, and in the case of the 0/90° layer order 60–70% [54–56]. Differences can also be caused by the molecular orientation and the difference in geometry and porosity between the filament and the 3D-printed samples. There was no significant difference in the crystalline fraction in this case. For the toughener-free material, the difference in strength between the filament and the 3D-printed samples is close to 40%, but for 5 wt% EBA-GMA content this decreases to 15%. The difference increases with the further increase of the elastomer content to 46% for 20 wt% EBA-GMA. Since the porosity of the 3D-printed samples varies between 17 and 27% depending on the EBA-GMA content, this, and the applied 0/90° printing layer order can explain the observed differences between the tensile strength of filaments and the 3D-printed samples with the same composition.

In the case of the tensile modulus such differences were not notable between the results of filaments and 3D-printed specimens (**Fig. 8/c**). This suggests that the load-bearing capacity of the bond between the rasters at the initial deformations, used to determine the modulus, is still adequate for all compositions.

The deformation at maximum force in the case of the filaments is 2–3

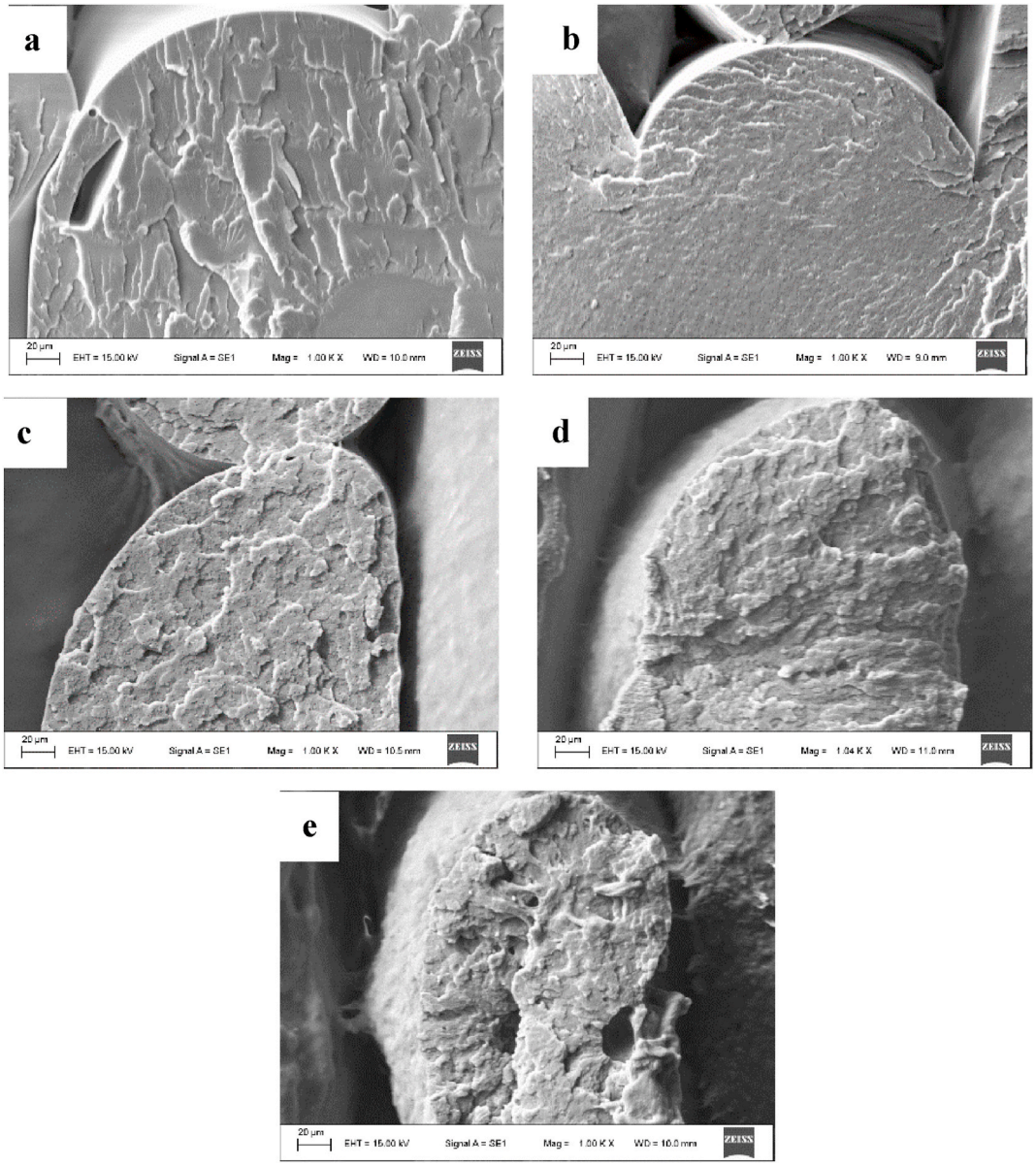

Fig. 6. SEM micrographs of fracture surface after unnotched impact test. 1000× magnification (**a:** RPET; **b:** RPET+5 wt% EBA-GMA; **c:** RPET+10 wt% EBA-GMA; **d:** RPET+15 wt% EBA-GMA; **e:** RPET+20 wt% EBA-GMA).

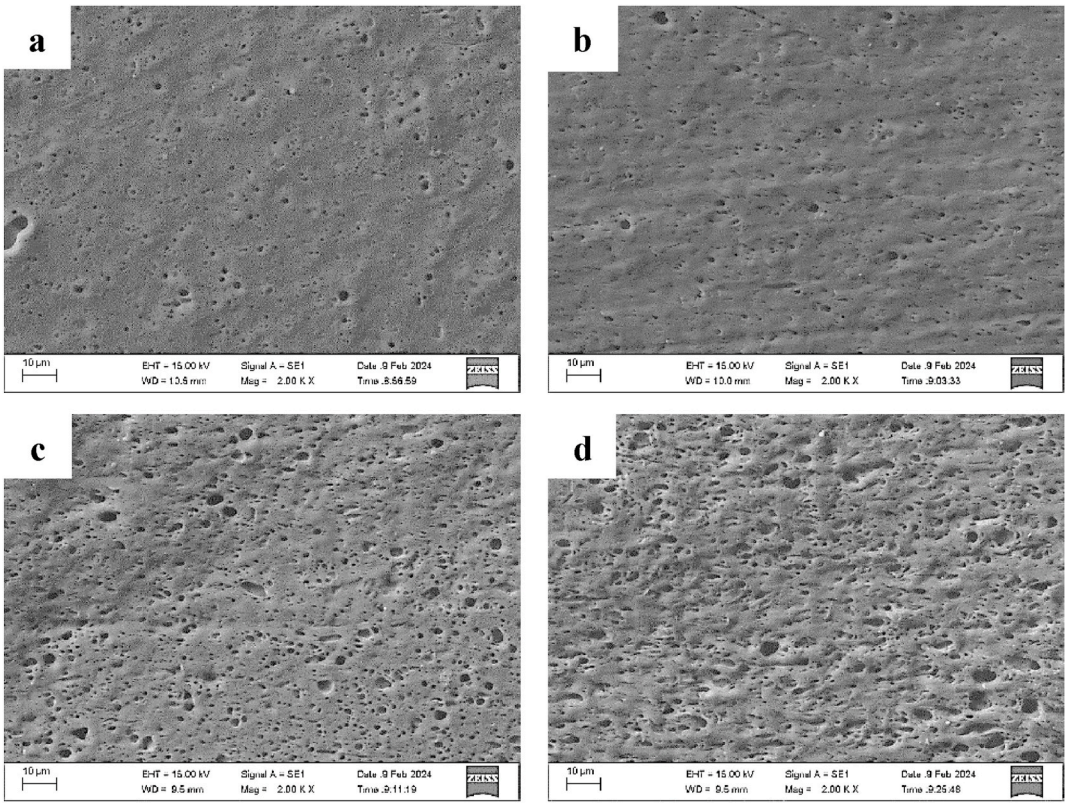

Fig. 7. SEM micrographs of 3D-printed specimens: 2000× magnification (**a**: RPET+5 wt% EBA-GMA; **b**: RPET+10 wt% EBA-GMA; **c**: RPET+15 wt% EBA-GMA; **d**: RPET+20 wt% EBA-GMA).

times higher than that of the 3D-printed samples (Fig. 8/**d**) for all compositions, so they suffered a larger plastic deformation. This is also primarily attributed to the 0/90° layer order during printing, as in the layers perpendicular to the load, the separation between the rasters is a more typical failure than the large radial deformation of the fibres.

This can also be seen in the SEM images taken of the fracture surfaces of 3D-printed samples after tensile test (Fig. 9). On these micrographs, it can be observed that the neat material shows a brittle fracture surface, which falls approximately in a plane. For this material, the elongation corresponding to the maximum force value was also small (2.2 and 1.7 % - Fig. 8/**d**). As the elastomer content increases, individual fibres deform more and more independently of each other, and the phenomenon of yielding can be observed more pronounced. The highest tensile strength of the 3D-printed samples is measured at 5 wt% EBA-GMA content, indicating that the best quality interlayer/raster bonding may be attributed to the lowest melting temperature (Fig. 2/**c**).

Fig. 10 illustrates the changes in flexural strength and modulus. The flexural moduli values are like the tensile moduli, and the linear descending of the values is quasi identical, too: at 20 wt% EBA-GMA content the stiffness of the 3D-printed specimens is reduced by half. The evolution of the flexural strength shows an exponential decreasing trend. At 10–20 wt% EBA-GMA content, the value of the flexural strength is in a similar range as the tensile strength (20–30 MPa) but at low elastomer contents (0–5 wt% EBA-GMA) it significantly exceeds this, reaching 45–60 MPa. In our previous research [35] samples with similar composition but manufactured by injection moulding were studied and their flexural strength was in the range of 50–100 MPa, decreasing with the elastomer content. Compared to this, a 40–60% reduction was observed in the case of 3D-printed samples, which can be explained by the anisotropy and the porosity of the specimens. Pictures taken after the flexural test are presented in Fig. 10/**c**. The failure is initiated from the bottom layers that undergo tensile stretching, however, the failure zone shows a change with the increase of the EBA-GMA content: in the sample without toughener, the damage is short in length, but penetrates deep into the cross-section, and the fracture is catastrophic and brittle with fibre breaks. With increasing elastomer content, the observable stress-whitening becomes longer and shallower, which indicates that the connection between the layers is weaker and load transfer is not effective in the case of larger deformations [57].

The temperature dependence of the storage modulus of 3D-printed samples is presented in the DMA curves shown in Fig. 11/**a**. It can be seen that the stiffness of the samples does not change significantly between 10 and 60 °C, but upon reaching the glass transition temperature (T_g) characteristic for PET, they soften in the range of 60–90 °C. The T_g temperature shows an increasing trend with the EBA-GMA content (Fig. 11/**b**), which supports that chemical bonds are formed between PET and EBA-GMA, that inhibit the mobility of PET molecules. This also contributes to the decrease in the MAF phase (see Fig. 2/e).

4. Conclusion

EBA-GMA elastomer was added to industrial-originated PET waste at different ratios, and after the compounding, filaments were produced from the developed materials and specimens were 3D-printed according to 0/90° layer order. With DSC and DMA measurements it was proved that the ratio of rigid amorphous phase increased with the elastomer content and the T_g values were higher too, which refer to chemical bonding between PET and EBA-GMA molecules, thus reactive compatibilization was achieved.

EBA-GMA reduces crystallinity in the case of rapid cooling applied during manufacturing but increases the shrinkage which results in lunkers in the deposited filaments and voids between the rasters.

The Izod impact strength of the 3D-printed samples greatly increased with the EBA-GMA content, in the case of 15 wt% elastomer the unnotched impact strength showed a 2.5-fold increase, while notched impact resistance reached a 9-fold increase compared to the neat,

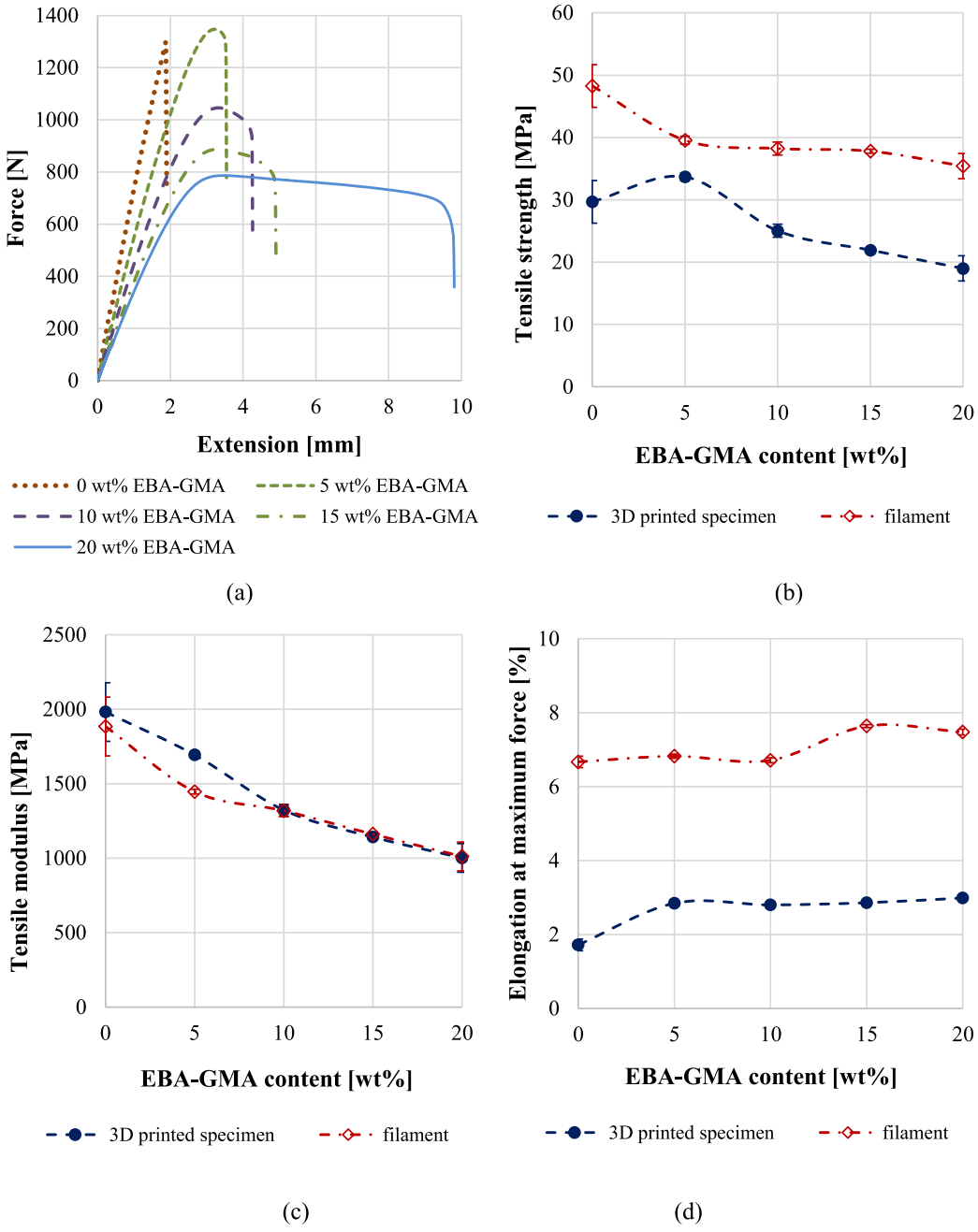

Fig. 8. Tensile test results: typical force-extension curves of 3D printed specimens (**a**); change of tensile strength (**b**); tensile modulus (**c**) and elongation at maximum force (**d**) as a function of EBA-GMA content.

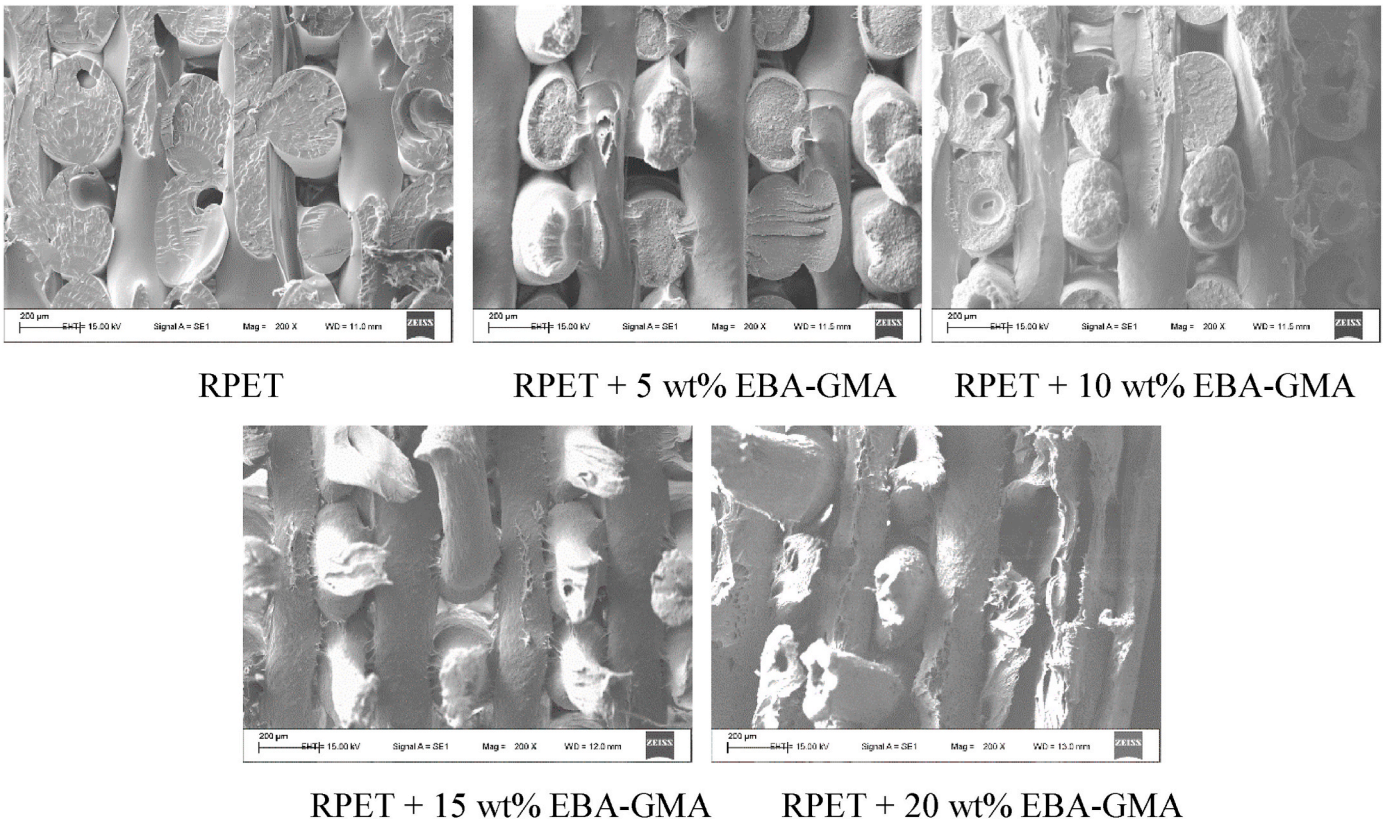

Fig. 9. SEM micrographs of fracture surface after tensile test.

recycled PET sample. Due to reactive compatibilization, the elastomer particles effectively increased the yielding in the recycled PET during failure, thus increasing the impact energy during the ductile fracture. The reactive compatibilization of EBA-GMA elastomer and thus its impact strength enhancing effect has also been demonstrated for poly (lactic acid) (PLA), which is also a key material for FFF 3D printing, but also has a brittle behaviour [58–60]. So based on our achievements, it could be a viable solution for additive manufacturing. It is also possible that other polyesters, such as poly(ethylene terephthalate) glycol (PETG), could also be used, thus supporting physical recycling.

During the quasi-static mechanical tests, the elastic modulus values determined in the initial phase of the load, at low forces and deformations, did not show significant difference from the filaments or the previously manufactured injection moulded samples [35] with similar compositions, however, the strength values fell behind. The reason besides the anisotropic structure is that the increment of the elastomer content results in weaker bonding between the layers and higher porosity. From this aspect, 3D-printed samples show some similarity with the self-reinforced PET composites, in which the bond between the layers also plays a major role in the evolution of the mechanical properties, which primarily depends on consolidation [61,62]. However, the application of the improved materials is limited by the decreasing modulus with increasing EBA-GMA content, which at 20 wt% is only 1 GPa, which is at the lower border of the range of polymers produced by the FFF process [63].

By changing the EBA-GMA content, the modulus-impact strength ratio of the printed samples can be tailored, so that the specifications given for a particular application can be satisfied. For example, while with 5 wt% EBA-GMA content 34 MPa tensile strength and 4 kJ/m^2 notched impact strength can be achieved, in the case of 15 wt% EBA-GMA, products with 22 MPa tensile strength and 12 kJ/m^2 notched impact strength can be manufactured with similar printing settings. As a reference, the abovementioned values were 16 MPa and 10 kJ/m^2 for 3D-printed ABS [64].

In conclusion, EBA-GMA is suitable for the toughening of recycled PET, and this effect can be still utilized after 3D printing. Thus, the biggest problem regarding the printing of recycled PET, brittleness, can be eliminated and parts with arbitrary geometry and balanced mechanical properties can be produced. The RPET/EBA-GMA blends may substitute ABS in various 3D printed products, such as in cases, electronic devices, and in individually designed applications. The price of PET waste, which is the raw material for the composites produced, especially of the lower quality fraction, is expected to continue to fall due to EU regulations promoting the circular economy, thus it is a promising raw material. In addition, the conversion of plastic waste into value-added feedstock may be more important than the short-term costs.

CRediT authorship contribution statement

Laszlo Toth: Methodology, Investigation. **Emese Slezák:** Writing – original draft, Visualization, Methodology, Investigation. **Katalin Bocz:** Writing – review & editing, Supervision. **Ferenc Ronkay:** Writing – original draft, Supervision, Methodology, Investigation, Conceptualization.

Declaration of competing interest

The authors declare that they have no known competing financial interests or personal relationships that could have appeared to influence the work reported in this paper.

Data availability

Data will be made available on request.

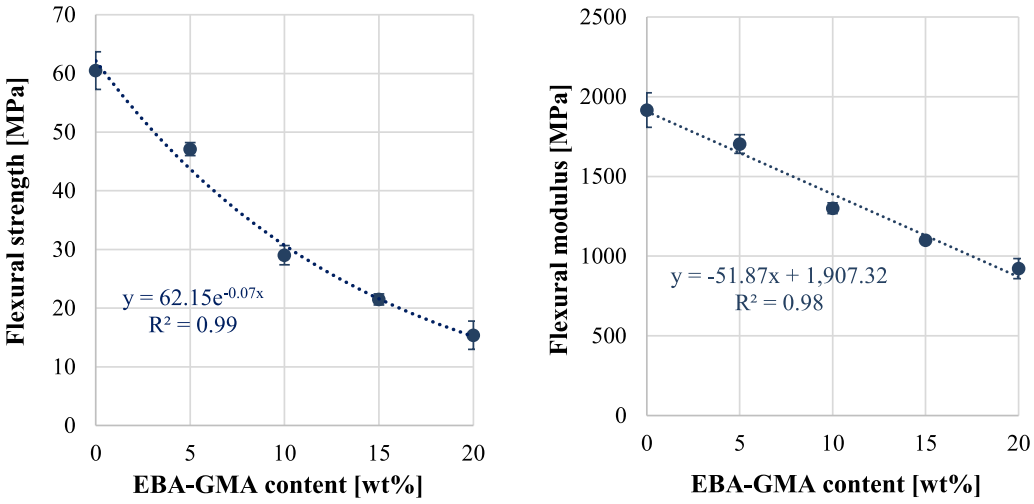

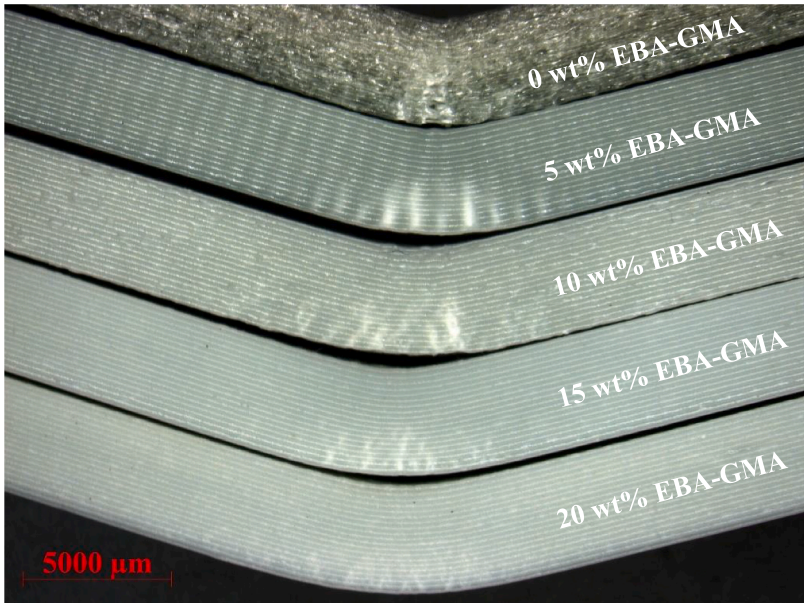

Fig. 10. Flexural strength (**a**); flexural modulus (**b**) and stereo-microscopic images after the test (**c**) with increasing EBA-GMA content.

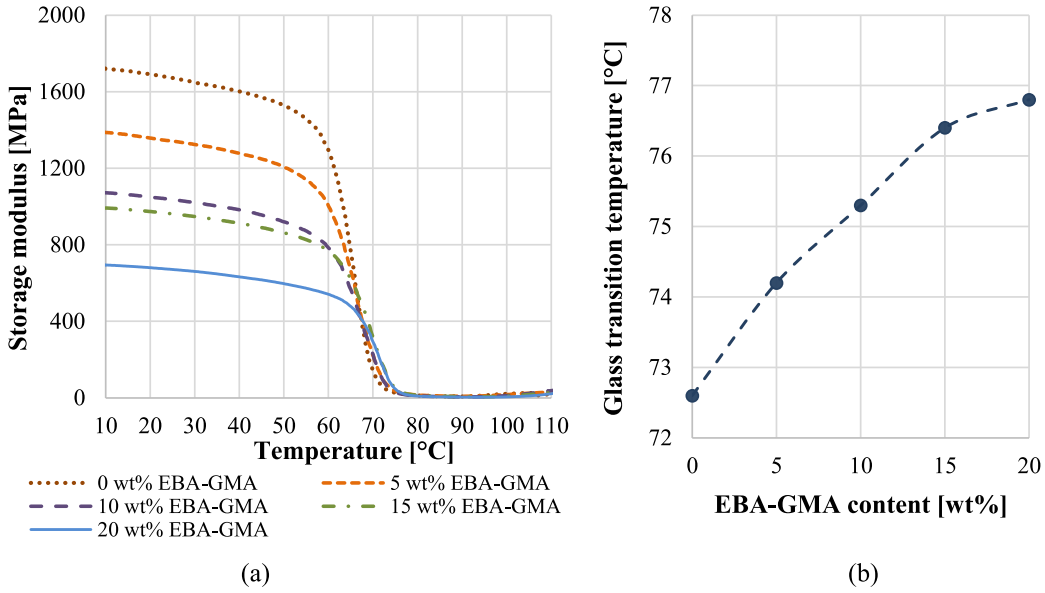

Fig. 11. DMA curves: temperature dependence of storage modulus (a) and glass transition temperature determined by DMA as a function of EBA-GMA content (b).

Acknowledgement

The project was funded by the National Research, Development and Innovation Fund of Hungary in the frame of the GINOP_PLUSZ-2.1.1-21-2022-00041 projects. The research was funded by the Sustainable Development and Technologies National Programme of the Hungarian Academy of Sciences (FFT NP FTA). E. Slezák expresses her gratitude for the project no. KDP-IKT-2023-900-I1-00000957/0000003, which has been implemented with the support provided by the Ministry of Culture and Innovation of Hungary from the National Research, Development and Innovation Fund, financed under the KDP-2023 funding scheme.

References

[1] G. Kónya, P. Ficzere, The effect of layer thickness and orientation of the Workpiece on the micro- and macrogeometric properties and the machining time of the part during 3D printing, Period. Polytech. - Mech. Eng. 67 (2023) 143–150, https://doi.org/10.3311/PPme.21473.
[2] M. Azlin, R. Ilyas, M. Zuhri, S. Sapuan, M. Harussani, S. Sharma, A. Nordin, N. Nurazzi, A. Afiqah, 3D printing and shaping polymers, composites, and nanocomposites: a review, Polymers 14 (2022) 180, https://doi.org/10.3390/polym14010180.
[3] K.R. Ryan, M.P. Down, N.J. Hurst, E.M. Keefe, C.E. Banks, Additive manufacturing (3D printing) of electrically conductive polymers and polymer nanocomposites and their applications, eScience 2 (2022) 365–381, https://doi.org/10.1016/j.esci.2022.07.003.
[4] K.R. Kunduru, R. Hogerat, K. Ghosal, M. Shaheen-Mualim, S. Farah, Renewable polyol-based biodegradable polyesters as greener plastics for industrial applications, Chem. Eng. J. 459 (2023) 141211, https://doi.org/10.1016/j.cej.2022.141211.
[5] B. Ádám, Z. Weltsch, Thermal and mechanical assessment of PLA-SEBS and PLA-SEBS-CNT biopolymer blends for 3D printing, Appl. Sci. 11 (2021) 6218, https://doi.org/10.3390/app11136218.
[6] R. Mantecón, C. Rufo-Martín, R. Castellanos, J. Diaz-Alvarez, Experimental assessment of thermal gradients and layout effects on the mechanical performance of components manufactured by fused deposition modeling, Rapid Prototyp. J. 28 (2022) 1598–1608, https://doi.org/10.1108/RPJ-12-2021-0329.
[7] J. Kechagias, S. Zaoutsos, Effects of 3D-printing processing parameters on FFF parts' porosity: outlook and trends, Mater. Manuf. Process. (2024) 1–11, https://doi.org/10.1080/10426914.2024.2304843.
[8] J.D. Kechagias, S.P. Zaoutsos, An investigation of the effects of ironing parameters on the surface and compression properties of material extrusion components utilizing a hybrid-modeling experimental approach, Progress in Additive Manufacturing (2023), https://doi.org/10.1007/s40964-023-00536-2.
[9] K. Gnanasekaran, T. Heijmans, S. van Bennekom, H. Woldhuis, S. Wijnia, G. de With, H. Friedrich, 3D printing of CNT- and graphene-based conductive polymer nanocomposites by fused deposition modeling, Appl. Mater. Today 9 (2017) 21–28, https://doi.org/10.1016/j.apmt.2017.04.003.
[10] G. Postiglione, G. Natale, G. Griffini, M. Levi, S. Turri, Conductive 3D microstructures by direct 3D printing of polymer/carbon nanotube nanocomposites via liquid deposition modeling, Compos Part A Appl Sci Manuf 76 (2015) 110–114, https://doi.org/10.1016/j.compositesa.2015.05.014.
[11] X. Zhou, J. Deng, C. Fang, W. Lei, Y. Song, Z. Zhang, Z. Huang, Y. Li, Additive manufacturing of CNTs/PLA composites and the correlation between microstructure and functional properties, J. Mater. Sci. Technol. 60 (2021) 27–34, https://doi.org/10.1016/j.jmst.2020.04.038.
[12] N. Lukács, F. Ronkay, B. Molnár, B. Marosfői, K. Bocz, Characterisation of flame retarded recycled PET foams produced by batch foaming, Polym. Test. 124 (2023), https://doi.org/10.1016/j.polymertesting.2023.108104.
[13] A. Bata, D. Nagy, Z. Weltsch, Effect of recycling on the mechanical, thermal and rheological properties of Polypropylene/carbon nanotube composites, Polymers 14 (2022) 5257, https://doi.org/10.3390/polym14235257.
[14] K. Mikula, D. Skrzypczak, G. Izydorczyk, J. Warchoł, K. Moustakas, K. Chojnacka, A. Witek-Krowiak, 3D printing filament as a second life of waste plastics-a review, (n.d.). https://doi.org/10.1007/s11356-020-10657-8/Published..
[15] H. Schneevogt, K. Stelzner, B. Yilmaz, B.E. Abali, A. Klunker, C. Völlmecke, Sustainability in additive manufacturing: exploring the mechanical potential of recycled PET filaments, Compos. Adv. Mater. 30 (2021) 263498332110000, https://doi.org/10.1177/26349833211000063.
[16] N.R. Madhu, H. Erfani, S. Jadoun, M. Amir, Y. Thiagarajan, N.P.S. Chauhan, Fused deposition modelling approach using 3D printing and recycled industrial materials for a sustainable environment: a review, Int. J. Adv. Des. Manuf. Technol. 122 (2022) 2125–2138, https://doi.org/10.1007/s00170-022-10048-y.
[17] N. Vidakis, M. Petousis, L. Tzounis, A. Maniadi, E. Velidakis, N. Mountakis, J. D. Kechagias, Sustainable additive manufacturing: mechanical response of Polyamide 12 over multiple recycling processes, Materials 14 (2021) 466, https://doi.org/10.3390/ma14020466.
[18] N. Vidakis, M. Petousis, A. Maniadi, Sustainable additive manufacturing: mechanical response of high-density polyethylene over multiple recycling processes, Recycling 6 (2021) 4, https://doi.org/10.3390/recycling6010004.
[19] N. Vidakis, M. Petousis, L. Tzounis, S.A. Grammatikos, E. Porfyrakis, A. Maniadi, N. Mountakis, Sustainable additive manufacturing: mechanical response of polyethylene terephthalate glycol over multiple recycling processes, Materials 14 (2021) 1162, https://doi.org/10.3390/ma14051162.
[20] N. Vidakis, M. Petousis, L. Tzounis, A. Maniadi, E. Velidakis, N. Mountakis, D. Papageorgiou, M. Liebscher, V. Mechtcherine, Sustainable additive manufacturing: mechanical response of polypropylene over multiple recycling processes, Sustainability 13 (2020) 159, https://doi.org/10.3390/su13010159.
[21] N. Vidakis, M. Petousis, A. Maniadi, E. Koudoumas, A. Vairis, J. Kechagias, Sustainable additive manufacturing: mechanical response of acrylonitrile-butadiene-styrene over multiple recycling processes, Sustainability 12 (2020) 3568, https://doi.org/10.3390/su12093568.
[22] M.K.J.E. Exconde, J.A.A. Co, J.Z. Manapat, E.R. Magdaluyo, Materials selection of 3D printing filament and utilization of recycled polyethylene terephthalate (PET) in a redesigned breadboard, in: Procedia CIRP, Elsevier B.V., 2019, pp. 28–32, https://doi.org/10.1016/j.procir.2019.04.337.
[23] M. Nikam, P. Pawar, A. Patil, A. Patil, K. Mokal, S. Jadhav, Sustainable fabrication of 3D printing filament from recycled PET plastic, Mater. Today Proc. (2023), https://doi.org/10.1016/j.matpr.2023.08.205.
[24] I. Tylman, K. Dzierzek, Filament for a 3D printer from pet bottles-simple machine, International Journal of Mechanical Engineering and Robotics Research 9 (2020) 1386–1392, https://doi.org/10.18178/ijmerr.9.10.1386-1392.

[25] N.E. Zander, M. Gillan, R.H. Lambeth, Recycled polyethylene terephthalate as a new FFF feedstock material, Addit. Manuf. 21 (2018) 174–182, https://doi.org/10.1016/j.addma.2018.03.007.
[26] A. Oussai, Z. Bártfai, L. Kátai, Development of 3d printing raw materials from plastic waste. A case study on recycled polyethylene terephthalate, Appl. Sci. 11 (2021), https://doi.org/10.3390/app11167338.
[27] A.L. Woern, D.J. Byard, R.B. Oakley, M.J. Fiedler, S.L. Snabes, J.M. Pearce, Fused particle fabrication 3-D printing: recycled materials' optimization and mechanical properties, Materials 11 (2018), https://doi.org/10.3390/ma11081413.
[28] H.A. Little, N.G. Tanikella, M.J. Reich, M.J. Fiedler, S.L. Snabes, J.M. Pearce, Towards distributed recycling with additive manufacturing of PET flake feedstocks, Materials 13 (2020), https://doi.org/10.3390/MA13194273.
[29] B. Pricop, Ștefan D. Sava, N.M. Lohan, L.G. Bujoreanu, DMA investigation of the factors influencing the glass transition in 3D printed specimens of shape memory recycled PET, Polymers 14 (2022), https://doi.org/10.3390/polym14112248.
[30] C.K. Ror, S. Negi, V. Mishra, Development and characterization of sustainable 3D printing filaments using post-consumer recycled PET: processing and characterization, J. Polym. Res. 30 (2023), https://doi.org/10.1007/s10965-023-03742-2.
[31] R. Singh, B.P. Singh, A.P. Singh, V. Kumar, R. Kumar, M. Bodaghi, A. Serjouei, Y. Wei, On 3D printing of low-cost sensors using recycled PET, (n.d.). https://doi.org/10.1007/s12046-022-02029-4S..
[32] R. Singh, B.P. Singh, A.P. Singh, S. Kumar, Y. Wei, Effect of infill density on the performance of recycled PET-based 3D printed microstrip antenna, Natl. Acad. Sci. Lett. 45 (2022) 525–529, https://doi.org/10.1007/s40009-022-01174-y.
[33] F. Ronkay, B. Molnar, D. Gere, T. Czigany, Plastic waste from marine environment: demonstration of possible routes for recycling by different manufacturing technologies, Waste Management 119 (2021) 101–110, https://doi.org/10.1016/j.wasman.2020.09.029.
[34] I. Fekete, F. Ronkay, L. Lendvai, Highly toughened blends of poly(lactic acid) (PLA) and natural rubber (NR) for FDM-based 3D printing applications: the effect of composition and infill pattern, Polym. Test. 99 (2021) 107205, https://doi.org/10.1016/j.polymertesting.2021.107205.
[35] K. Bocz, F. Ronkay, K.E. Decsov, B. Molnár, G. Marosi, Application of low-grade recyclate to enhance reactive toughening of poly(ethylene terephthalate), Polym. Degrad. Stabil. 185 (2021), https://doi.org/10.1016/j.polymdegradstab.2021.109505.
[36] F. Ronkay, B. Molnár, E. Szabó, G. Marosi, K. Bocz, Water boosts reactive toughening of PET, Polym. Degrad. Stabil. 203 (2022), https://doi.org/10.1016/j.polymdegradstab.2022.110052.
[37] E. Slezák, F. Ronkay, K. Bocz, Development of an engineering material with increased impact strength and heat resistance from recycled PET, J. Polym. Environ. (2023), https://doi.org/10.1007/s10924-023-02945-4.
[38] S. Chang, M.-F. Sheu, S.-M. Chen, Solid-state polymerization of poly(ethylene terephthalate), J. Appl. Polym. Sci. 28 (1983) 3289–3300, https://doi.org/10.1002/app.1983.070281023.
[39] O. Bouzaglou, O. Golan, N. Lachman, Process design and parameters interaction in material extrusion 3D printing: a review, Polymers 15 (2023) 2280, https://doi.org/10.3390/polym15102280.
[40] J. Chen, X. Liu, Y. Tian, W. Zhu, C. Yan, Y. Shi, L.B. Kong, H.J. Qi, K. Zhou, 3D-Printed anisotropic polymer materials for functional applications, Adv. Mater. 34 (2022), https://doi.org/10.1002/adma.202102877.
[41] A.Y. Al-Maharma, S.P. Patil, B. Markert, Effects of porosity on the mechanical properties of additively manufactured components: a critical review, Mater. Res. Express 7 (2020) 122001, https://doi.org/10.1088/2053-1591/abcc5d.
[42] H. Nouri, S. Guessasma, S. Belhabib, Structural imperfections in additive manufacturing perceived from the X-ray micro-tomography perspective, J. Mater. Process. Technol. 234 (2016) 113–124, https://doi.org/10.1016/j.jmatprotec.2016.03.019.
[43] J.D. Badia, E. Strömberg, S. Karlsson, A. Ribes-Greus, The role of crystalline, mobile amorphous rigid amorphous fractions in the performance of recycled poly (ethylene terephthalate) (PET), Polym. Degrad. Stabil. 97 (2012) 98–107, https://doi.org/10.1016/j.polymdegradstab.2011.10.008.
[44] F. Ferrari, C. Esposito Corcione, F. Montagna, A. Maffezzoli, 3D printing of polymer waste for improving people's awareness about marine litter, Polymers 12 (2020) 1738, https://doi.org/10.3390/polym12081738.
[45] B. Van de Voorde, A. Katalagarianakis, S. Huysman, A. Toncheva, J.-M. Raquez, I. Duretek, C. Holzer, L. Cardon, K.V. Bernaerts, D. Van Hemelrijck, L. Pyl, S. Van Vlierberghe, Effect of extrusion and fused filament fabrication processing parameters of recycled poly(ethylene terephthalate) on the crystallinity and mechanical properties, Addit. Manuf. 50 (2022) 102518, https://doi.org/10.1016/j.addma.2021.102518.
[46] C. Gupta, P. Mb, N.K. Shet, A.K. Ghosh, S. Bandyopadhyay, P. Mukhopadhyay, Microstructure and mechanical performance examination of 3D printed acrylonitrile butadiene styrene thermoplastic parts, Polym. Eng. Sci. 60 (2020) 2770–2781, https://doi.org/10.1002/pen.25507.
[47] Ö. Keleş, E.H. Anderson, J. Huynh, J. Gelb, J. Freund, A. Karakoç, Stochastic fracture of additively manufactured porous composites, Sci. Rep. 8 (2018) 15437, https://doi.org/10.1038/s41598-018-33863-4.
[48] S. Jang, A. Boddorff, D.J. Jang, J. Lloyd, K. Wagner, N. Thadhani, B. Brettmann, Effect of material extrusion process parameters on filament geometry and inter-filament voids in as-fabricated high solids loaded polymer composites, Addit. Manuf. 47 (2021) 102313, https://doi.org/10.1016/j.addma.2021.102313.
[49] X. Sun, M. Mazur, C.-T. Cheng, A review of void reduction strategies in material extrusion-based additive manufacturing, Addit. Manuf. 67 (2023) 103463, https://doi.org/10.1016/j.addma.2023.103463.
[50] E.A. Papon, A. Haque, S.B. Mulani, Process optimization and stochastic modeling of void contents and mechanical properties in additively manufactured composites, Compos. B Eng. 177 (2019) 107325, https://doi.org/10.1016/j.compositesb.2019.107325.
[51] F. Ronkay, B. Molnár, E. Szabó, G. Marosi, K. Bocz, Water boosts reactive toughening of PET, Polym. Degrad. Stabil. 203 (2022), https://doi.org/10.1016/j.polymdegradstab.2022.110052.
[52] E. Slezák, F. Ronkay, K. Bordácsné Bocz, Improvement of mechanical properties of recycled PET by reactive toughening and post-crystallization, Acta Technica Jaurinensis 15 (2022) 193–198, https://doi.org/10.14513/actatechjaur.00680.
[53] H.-H. Tsai, S.-J. Wu, Y.-D. Wu, W.-Z. Hong, Feasibility study on the fused filaments of injection-molding-grade poly(ethylene terephthalate) for 3D printing, Polymers 14 (2022) 2276, https://doi.org/10.3390/polym14112276.
[54] S. Ziemian, M. Okwara, C.W. Ziemian, Tensile and fatigue behavior of layered acrylonitrile butadiene styrene, Rapid Prototyp. J. 21 (2015) 270–278, https://doi.org/10.1108/RPJ-09-2013-0086.
[55] K. Fayazbakhsh, M. Movahedi, J. Kalman, The impact of defects on tensile properties of 3D printed parts manufactured by fused filament fabrication, Mater. Today Commun. 18 (2019) 140–148, https://doi.org/10.1016/j.mtcomm.2018.12.003.
[56] S. Ahn, M. Montero, D. Odell, S. Roundy, P.K. Wright, Anisotropic material properties of fused deposition modeling ABS, Rapid Prototyp. J. 8 (2002) 248–257, https://doi.org/10.1108/13552540210441166.
[57] S.R. Rajpurohit, H.K. Dave, Flexural strength of fused filament fabricated (FFF) PLA parts on an open-source 3D printer, Adv. Manuf. 6 (2018) 430–441, https://doi.org/10.1007/s40436-018-0237-6.
[58] N. Lukács, K.E. Decsov, B. Molnár, F. Ronkay, K. Bordácsné Bocz, Increased processing temperature assisted reactive toughening of poly(lactic acid), Express Polym. Lett. 17 (2023) 169–180, https://doi.org/10.3144/expresspolymlett.2023.12.
[59] Y. Yuryev, A.K. Mohanty, M. Misra, A new approach to supertough poly(lactic acid): a high temperature reactive blending, Macromol. Mater. Eng. 301 (2016) 1443–1453, https://doi.org/10.1002/mame.201600242.
[60] H. Liu, F. Chen, B. Liu, G. Estep, J. Zhang, Super toughened poly(lactic acid) ternary blends by simultaneous dynamic vulcanization and interfacial compatibilization, Macromolecules 43 (2010) 6058–6066, https://doi.org/10.1021/ma101108g.
[61] C. Wu, W. Lai, Mechanical and open hole tensile properties of self-reinforced PET composites with recycled PET fiber reinforcement, J. Appl. Polym. Sci. 133 (2016), https://doi.org/10.1002/app.43682.
[62] J.C. Chen, C.M. Wu, F.C. Pu, C.H. Chiu, Fabrication and mechanical properties of self-reinforced poly(ethylene terephthalate) composites, Express Polym. Lett. 5 (2011) 228–237, https://doi.org/10.3144/expresspolymlett.2011.22.
[63] J.R.C. Dizon, A.H. Espera, Q. Chen, R.C. Advincula, Mechanical characterization of 3D-printed polymers, Addit. Manuf. 20 (2018) 44–67, https://doi.org/10.1016/j.addma.2017.12.002.
[64] A.P. Agrawal, V. Kumar, J. Kumar, P. Paramasivam, S. Dhanasekaran, L. Prasad, An investigation of combined effect of infill pattern, density, and layer thickness on mechanical properties of 3D printed ABS by fused filament fabrication, Heliyon 9 (2023) e16531, https://doi.org/10.1016/j.heliyon.2023.e16531.